

# We are IntechOpen, the world's leading publisher of Open Access books Built by scientists, for scientists

6,900

Open access books available

186,000

International authors and editors

200M

Downloads

Our authors are among the

154

Countries delivered to

TOP 1%

most cited scientists

12.2%

Contributors from top 500 universities



WEB OF SCIENCE™

Selection of our books indexed in the Book Citation Index  
in Web of Science™ Core Collection (BKCI)

Interested in publishing with us?  
Contact [book.department@intechopen.com](mailto:book.department@intechopen.com)

Numbers displayed above are based on latest data collected.  
For more information visit [www.intechopen.com](http://www.intechopen.com)



# Elastic and Nanowearing Properties of SiO<sub>2</sub>-PMMA and Hybrid Coatings Evaluated by Atomic Force Acoustic Microscopy and Nanoindentation

J. Alvarado-Rivera<sup>1</sup>, J. Muñoz-Saldaña<sup>2</sup> and R. Ramírez-Bon<sup>2</sup>

<sup>1</sup>*Departamento de Investigación en Física, Universidad de Sonora*

<sup>2</sup>*Centro de Investigación y de Estudios Avanzados del IPN, Unidad Querétaro  
Mexico*

## 1. Introduction

Organic-inorganic hybrid materials have been widely studied during the past two decades. The capability to combine materials which are completely different has expanded the number of new materials with unique properties that are possible to synthesize. Thus, hybrid materials are nanocomposites where at least one of the components has a domain size of at least several nm [Sanchez, 1994]. In 1985, the first hybrid material was synthesized by the sol-gel process, combining alkoxides with organic monomers or oligomers leading to a hybrid network [Huang et al., 1985; Schmidt, 1985]. At this respect, sol-gel is a feasible, simple and low-cost technique. The hybrid materials obtained are polydisperse in size and locally heterogeneous in chemical composition [Sanchez et al., 2005]. These hybrids are also inexpensive, versatile and present many interesting applications converting them into marketable products as films, powders or monoliths. Among the wide variety of hybrid materials, SiO<sub>2</sub>-Poly(methylmethacrylate) (SiO<sub>2</sub>-PMMA), hybrids have shown interesting properties as higher hardness than some common thermoplastics like poly(methyl methacrylate), poly(ethylene terephthalate) and poly(ethylene naphthalate); low surface roughness; low friction coefficient; and high optical transparency. These properties are attractive to be applied as protective coatings as well as in the fabrication of electronic devices on flexible substrates like OLED's used as both planarization and insulator coatings. Plastic surface roughness lower than 2 nm are required in order to start deposition of ceramic films to assemble the device. This ultra-smooth surface can be achieved by hybrid coatings due to the combination of components at a molecular level. Moreover, SiO<sub>2</sub>-PMMA hybrids are flexible, a property conferred by the organic component, and thus they can undergo higher deformations before cracking if applied on plastic substrates.

Mechanical property evaluation using conventional mechanical testing is not suitable to evaluate mechanical properties of thin films, but instrumented indentation has provided a viable method. In nanoindentation, the surface of a material of unknown properties is indented at high spatial resolution with another material of known properties (such as diamond) while load and displacement is continuously recorded [Fischer-Cripps, 2004; Hay

& Pharr, 2000]. The load-displacement curves obtained from the test are used to determine elastic modulus and hardness by applying the method developed by Oliver and Pharr [Oliver & Pharr, 1992]. Moreover, nanoindentation also allows performance of wear tests at nanometric scale on thin films. Nanowells can be “machined” by the indenter applying a normal force. Then the wear resistance can be evaluated in terms of the wear loss volume, which is obtained by image analysis [Alvarado-Rivera et al., 2007, 2010].

As mentioned above, organic and inorganic phases are bonded at a molecular scale, and consequently the obtained films are optically transparent. Thus it is difficult to observe the distribution of both phases using conventional scanning electron microscopy. However, atomic force acoustic microscopy is a technique that offers the ability to observe a material's phase distribution at the surface by measuring the difference in elastic properties. Amplitude vibration of the surface is mapped by a cantilever (excited at a fixed frequency near its resonance). Depending on the variations of the local contact stiffness, resonance frequency will vary, causing the amplitude vibration of the work frequency to change, which will be reflected in contrast differences on the amplitude images [Rabe, 2006; Kopycinska-Müller et al., 2007]. In this chapter, the elastic and viscoelastic behaviour, hardness and nanowear characterization of SiO<sub>2</sub>-PMMA hybrid coatings by atomic force acoustic microscopy (AFAM) imaging and nanoindentation are presented and discussed.

## 2. Wear behaviour of SiO<sub>2</sub>-PMMA hybrid coatings reinforced with Al<sub>2</sub>O<sub>3</sub> whiskers and nanoparticles

### 2.1 Materials preparation and experimental set-up

For the sol-gel synthesis of the hybrid coatings, tetraethylortosilicate (TEOS) and methyl methacrylate (MMA) were used as silica and polymethyl methacrylate (PMMA) precursors. To crosslink both phases, 3-Trimetoxisilylpropyl methacrylate was added to the precursor formulation. The TEOS:MMA:TMSPM molar ratio was chosen according to the enhanced mechanical properties of the hybrid coatings obtained with this precursor composition. In this study the effect of Al<sub>2</sub>O<sub>3</sub> nanoparticles and nanowhiskers on the hybrid coatings was analysed. Four hybrid solutions with different content of Al<sub>2</sub>O<sub>3</sub> nanoparticles and whiskers were prepared. Details of the combinations are shown in Table 1. The alumina nanoparticles (pAl<sub>2</sub>O<sub>3</sub>) and whiskers (wAl<sub>2</sub>O<sub>3</sub>) were provided as nanopowders. The nanoparticles have an average size of 50 nm with a superficial area of 33 m<sup>2</sup>/g. The whiskers have a diameter of 2-4 nm and a length of 2800nm. This information was provided by the supplier, Sigma-Aldrich.

Sample	TEOS:MMA:TMSPM (Molar ratio)	Al <sub>2</sub> O <sub>3</sub> Nanoparticles (wt. %)	Al <sub>2</sub> O <sub>3</sub> Whiskers (wt.%)
SiO <sub>2</sub> -PMMA	1:0.25:0.25	0	0
SiO <sub>2</sub> -PMMA- 0.05pAl <sub>2</sub> O <sub>3</sub>	1:0.25:0.25	0.05	0
SiO <sub>2</sub> -PMMA- 0.1pAl <sub>2</sub> O <sub>3</sub>	1:0.25:0.25	0.1	0
SiO <sub>2</sub> -PMMA- 0.1wAl <sub>2</sub> O <sub>3</sub>	1:0.25:0.25	0	0.1

Table 1. Details of the prepared solutions.

Al<sub>2</sub>O<sub>3</sub> nanoparticles and whiskers were added in a beaker with deionized water and then placed into an ultrasonic bath for 20 minutes to aid dispersion. TEOS was mixed with the deionized water containing the nanoparticles or the whiskers, then ethanol and chlorhidric acid (HCl) as a catalyst were added and mixed together for 30 minutes. The MMA precursor solution was prepared by adding benzoil peroxide to promote radical polymerization. The crosslinking agent was also mixed with deionized water and ethanol to hydrolyse the metoxy groups of the molecule. Afterwards, the three precursor solutions were mixed together in a molar ratio of TEOS:MMA:TMSPM of 1:0.25:0.25 and then the solution was stirred for 30 minutes. The solutions were left to age for one day. Sets of Corning glass and commercial acrylic substrates were coated with the four different hybrid solutions by dip coating. Finally, the coated substrates were dried in a conventional oven at 70°C for 6 hours.

### 2.1.1 Nanoindentation testing

Nanoindentation or instrumented indentation is a technique, which basically consists of indenting a material of unknown properties and continuously recording the applied load and displacement with high spatial resolution [Hay & Pharr, 2000]. In this technique it is essential to have a material of known properties for the calibration of the measurement system prior to the analysis. All the nanoindentation tests and nanowearing testing were performed on a Hysiton Ubi-1 nanoindenter (Minneapolis, MN) equipped with a Berkovich diamond tip. In Fig. 1 a schematic representation of the nanoindentation set-up is presented. The equipment is provided with a piezoelectric actuator, which precisely moves the tip before and after the test. The system is able to record images of the sample surface before and after the indentation and perform scratch testing using the same diamond tip used for indentation. The force/displacement transducer (shown in Fig. 1) consists of an arrangement of three capacitive plates, with the tip attached to a beam that is fixed to the central plate. The force is administered by applying a voltage to the bottom capacitor, creating an electrostatic attraction between the bottom and central plate, and moving the central plate towards the bottom. The magnitude of the force is calculated from the applied voltage. The load-displacement curves (*P-h*) obtained from the indentation test (an example is depicted in Fig. 1) are used to extract the hardness and elastic modulus of the indented material using the method introduced by Oliver and Pharr [Oliver & Pharr, 1992]. A simple load-unload cycle was used to perform the indentation test on the hybrid coatings. Several indents were applied varying the load from 50 μN to 9 mN . Since the hardness calculated from the *P-h* curves is the hardness of the substrate/film system, the work-of-indentation model was applied to extract the film hardness [Korsunsky et al., 1998]. This method describes the behaviour of the hardness over a wide range, and it can be applied to systems with either fracture or plastic deformation. The method is described by the following equation:

$$H_c = H_s + \frac{H_f - H_s}{1 + k\beta^2} \quad (1)$$

where  $H_c$  is the composite hardness (substrate/film system);  $H_s$  and  $H_f$  are the substrate and film hardness, respectively; and  $k$  is a constant. In order to apply this equation to fit the experimental data, it is necessary to plot  $H_c$  as a function of the relative indentation depth,  $\beta = h/t$ , which is the penetration depth ( $h$ ) divided by the film thickness ( $t$ ). The film thickness of all hybrid coated glass and acrylic were determined using a Dektak II profilometer.

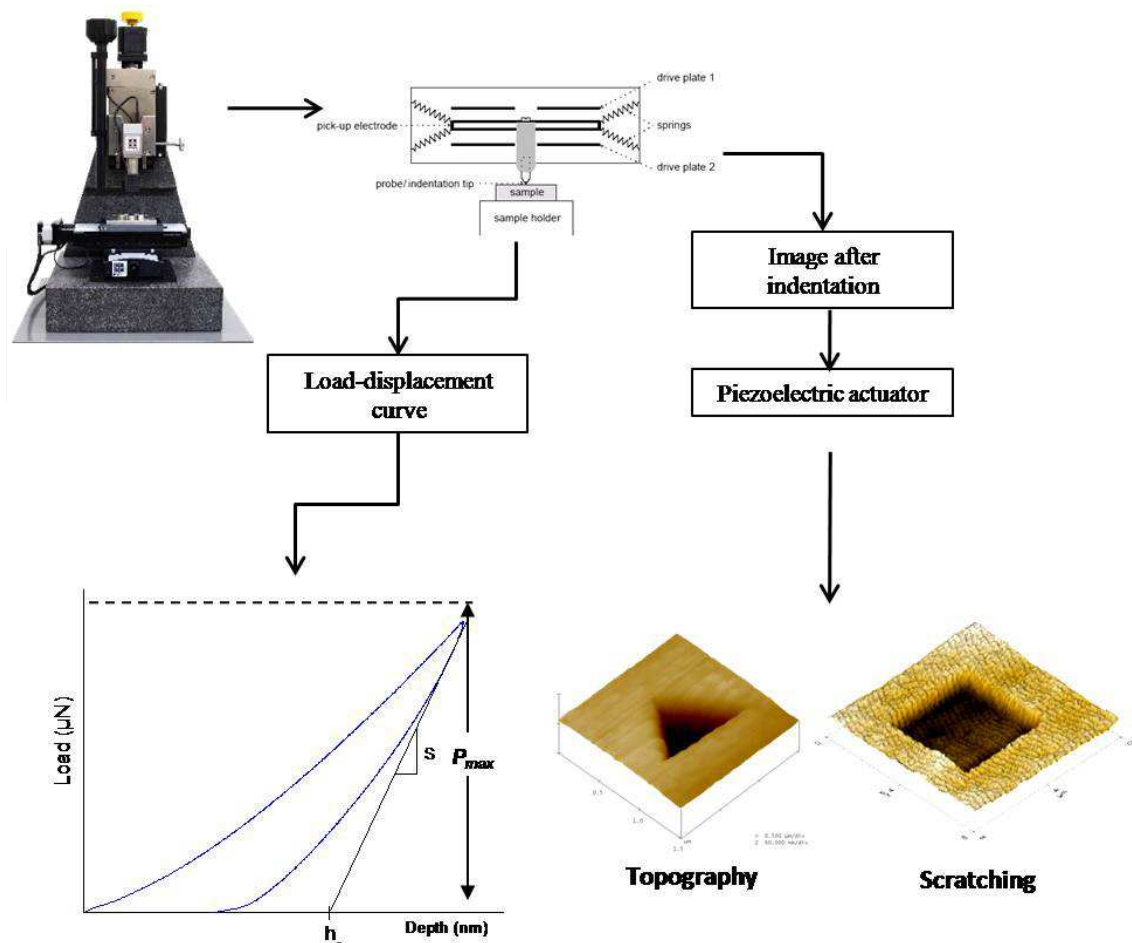


Fig. 1. Schematic representation of the Hysitron-Ubi-1 nanoindentation system.

### 2.1.2 Sliding life test

Sliding life tests were carried out on a pin-on disc tribometer (CSM Instruments) using a 10 mm diameter steel pin and applying a normal force of 1 N without the aid of lubricant. The test consists of the steel pin sliding on the sample surface at a constant velocity, and the instantaneous friction coefficient is recorded as a function of the covered distance. For the hybrid coatings a velocity of 1 cm/s was used.

### 2.1.3 Nanowear

Nanoscratch testing was performed with the Hysitron Ubi-1 nanoindenter by machining nanometric cavities on the coating surface using the Berkovich diamond tip. A fixed area of  $6 \times 6 \mu\text{m}$  was scanned ten times applying a normal load of  $70 \mu\text{N}$  at a frequency of 1 Hz. In Fig. 2 a schematic representation of the nanoscratch test is presented. The diamond tip moves along the x-axis removing material; after the scratching is finished an image of the surface is then taken. Afterwards, the images of the nanowells were analyzed using WSxM (software) to determine the material wear loss volume [Horcas et al., 2007]. The borders of the wells are irregular due to the tip geometry, thus with image analysis is possible to determine the real borders of the hole and the volume of the wells using the command flooding, which can detect holes and hills on the image establishing a reference height.

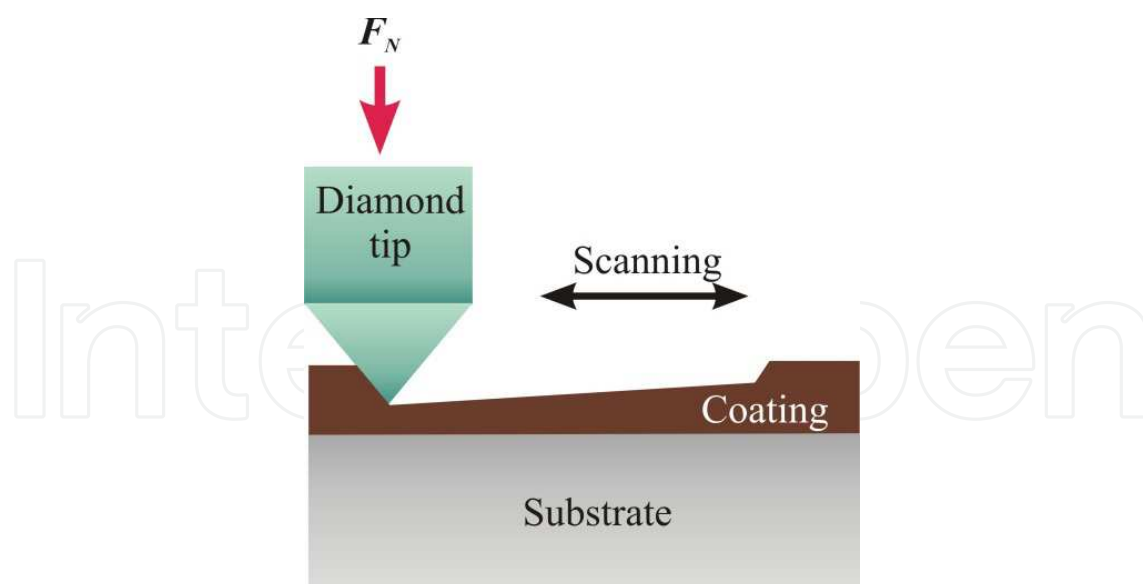


Fig. 2. Schematic representation of nanoscratch testing on the sample surface performed by the nanoindenter diamond tip.

## 2.2 Hybrid optical characterization

Fig. 3 shows the UV-Vis optical transmission of the studied hybrid coatings and acrylic substrate for comparison. It is observed that the acrylic substrate has about 92 %, on average, optical transmission in the visible range. All hybrid coatings clearly show higher optical transmittance than the substrate in the visible region. There is no evidence of light dispersion due to the incorporated nanoparticles or whiskers. The oscillations observed in the spectra of the hybrid layers are due to interference produced because the coating thickness is of the order of the incident wavelength. The high optical transparency of the hybrid coatings evidences that there is no phase separation in the hybrid materials, and therefore they are homogeneous, showing incorporated organic and inorganic phases.

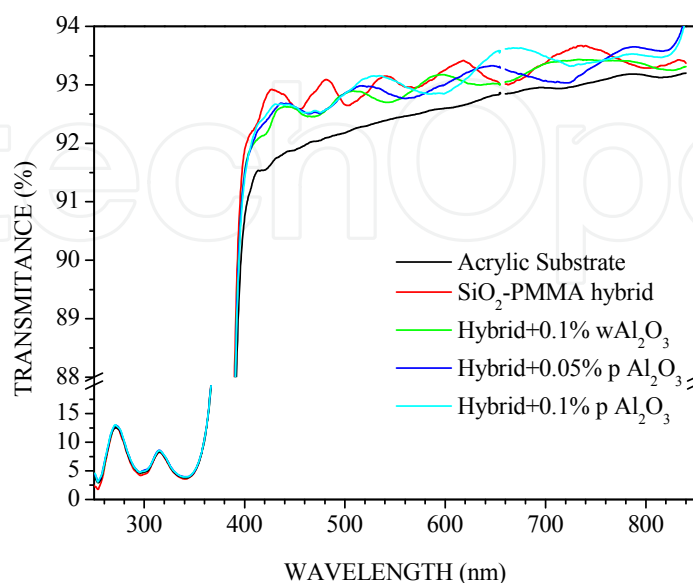


Fig. 3. Optical transmission spectra of the hybrid coatings and the acrylic substrate.

### 2.3 Nanoindentation hardness

A series of at least 25 indentations in the range load of 30 to 6000  $\mu\text{N}$  were performed on each type of hybrid coating, and uncoated acrylic substrate was also tested. For comparison a Corning glass slice was coated with the hybrid solution with 0.1 wt.% alumina whiskers. The composite hardness ( $H_c$ ) as a function of the relative indentation depth of the hybrid coatings is displayed in Fig. 4. In all cases the curves show the characteristic form of a hard coating on a soft substrate system. In Fig. 4 a) the coatings with alumina nanoparticles and the hybrid coating without alumina are compared. The continuous line for each set of data corresponds to the work of indentation model fitting to estimate the film hardness ( $H_f$ ). The hardness of the coatings with 0.05 and 0.1 wt.% were similar to that of the  $\text{SiO}_2$ -PMMA coating. However these values are higher than that of the acrylic substrate of 0.17 GPa, also measured by nanoindentation. The hybrid coating with alumina nanowhiskers on the acrylic substrate showed the lowest values of hardness of 0.512 GPa (Table 2). However, the same coating on the glass substrates showed the highest hardness value of 0.814 GPa. This difference can be attributed to the substrate itself, since glass is much harder than PMMA. Thus, when the coating/acrylic substrate system is under load the coating deformation volume also includes the substrate, and its elastic properties contribute to the final measurement of the penetration depth, and consequently the hardness and reduced modulus. In the case of the coating on glass, the substrate has a high elastic modulus and is harder than the coating, and thus the deformation volume under the indenter is confined within the coating [Fischer-Cripps, 2004].

### 2.4 Sliding life testing

All the hybrid coatings were tested to determine their sliding life and friction coefficient. The results for the coatings with better performance are shown in Fig. 5; the others failed in early stages of the test. The coatings that showed more resistance for the test were those with alumina nanowhiskers with a friction coefficient lower than that of the acrylic substrate. The coating with the best performance was  $\text{SiO}_2$ -PMMA-0.1w $\text{Al}_2\text{O}_3$  on glass, while the same coating on acrylic started to fail after 4 m of sliding. This can be explained in terms of the differences in elastic properties of the substrates in the same way that occurs for the hardness explained in the previous section. For this test, a pin with a 10 mm of radius applying a normal load of 1N is in contact with the coating surface. The size of the pin and the applied load are high enough to generate a large deformation volume within the substrate, affecting the coating which is also being subjected to wear. It is worth to mention that this coating on acrylic resisted more than the hybrid without alumina whiskers also on acrylic, thus alumina whiskers provide reinforcement in terms of enhancing the wear resistance of the  $\text{SiO}_2$ -PMMA hybrid material.

The hybrid-whisker coating on glass resisted the test without failing after 40 m of sliding, but it showed some abrupt increments of the friction coefficient. As the sliding contact between the surfaces continues the material adhered to the pin is detached and transferred to the coating surface by cold welding causing a drop in  $\mu$  values. Optical photomicrographs of the wear zone on the hybrid surfaces were taken and they are displayed in Fig. 6. For hybrid coatings both with and without whiskers on acrylic substrate, zones with removed material, caused by fracture of the coating surface, are visible. The generated debris promotes abrasive wear between the sliding surfaces (increasing friction) and, thus, the

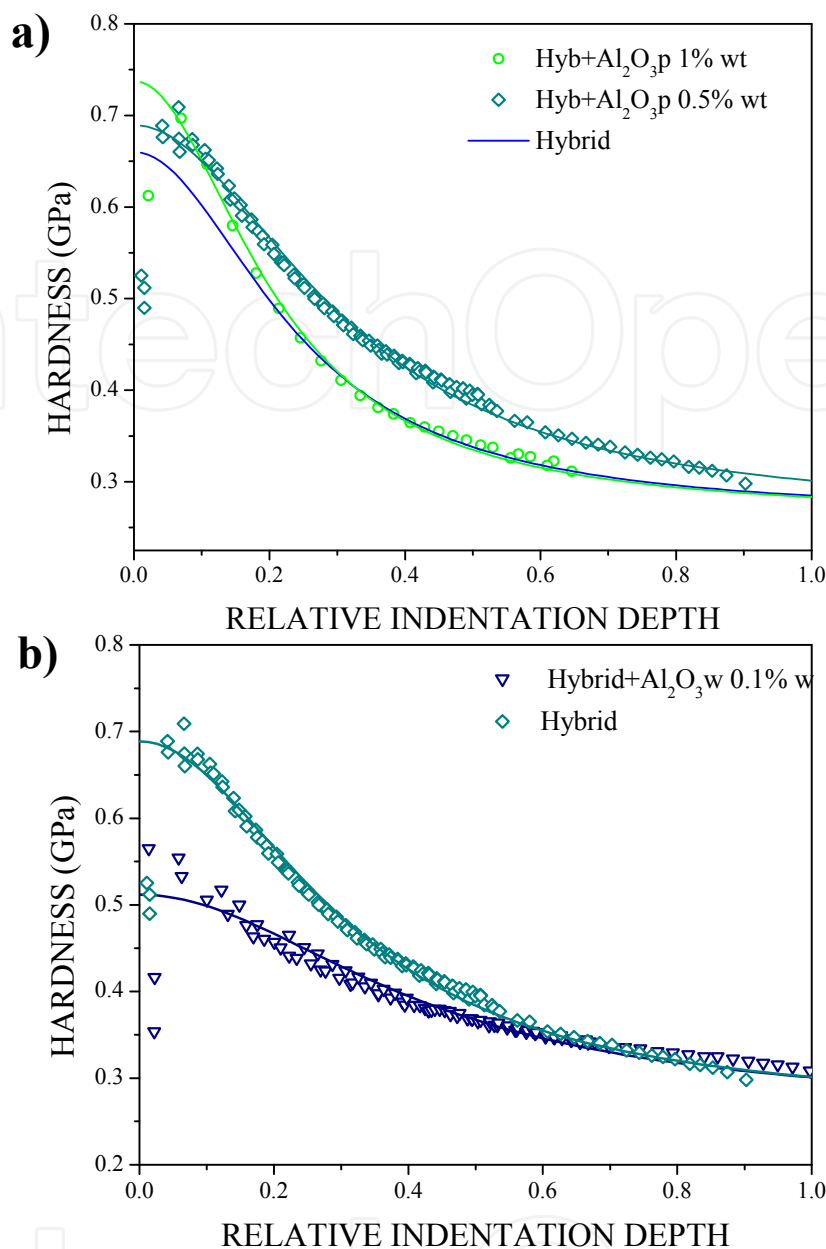


Fig. 4. Composite hardness as a function of the relative indentation depth of the hybrid coatings on acrylic: a) Al<sub>2</sub>O<sub>3</sub> nanoparticles and b) Al<sub>2</sub>O<sub>3</sub> whiskers.

Sample	Film Hardness (GPa)
Hybrid SiO <sub>2</sub> -PMMA	0.689
Hybrid+0.05% pAl <sub>2</sub> O <sub>3</sub>	0.66
Hybrid+0.1% pAl <sub>2</sub> O <sub>3</sub>	0.738
Hybrid+0.1% wAl <sub>2</sub> O <sub>3</sub> on Acrylic	0.512
Hybrid+0.1% wAl <sub>2</sub> O <sub>3</sub> on glass	0.814

Table 2. Film hardness of all hybrid coatings.

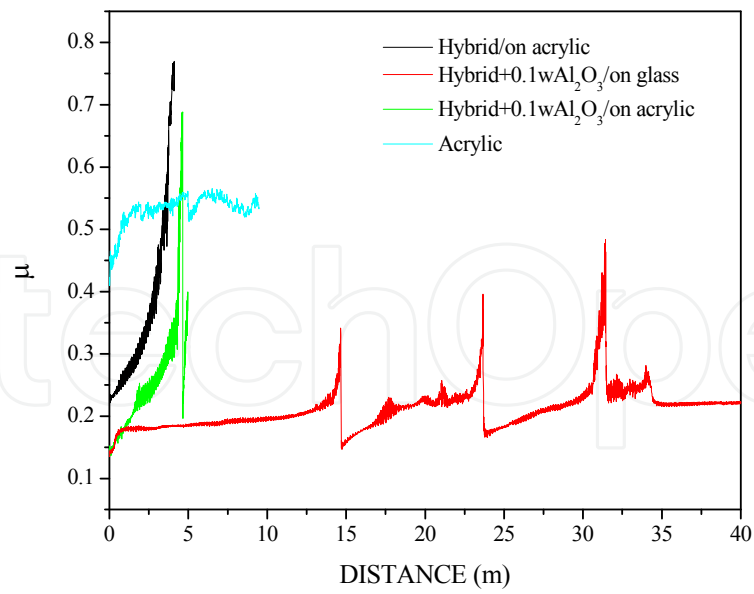


Fig. 5. Sliding life test of the hybrid coatings with and without reinforcement.

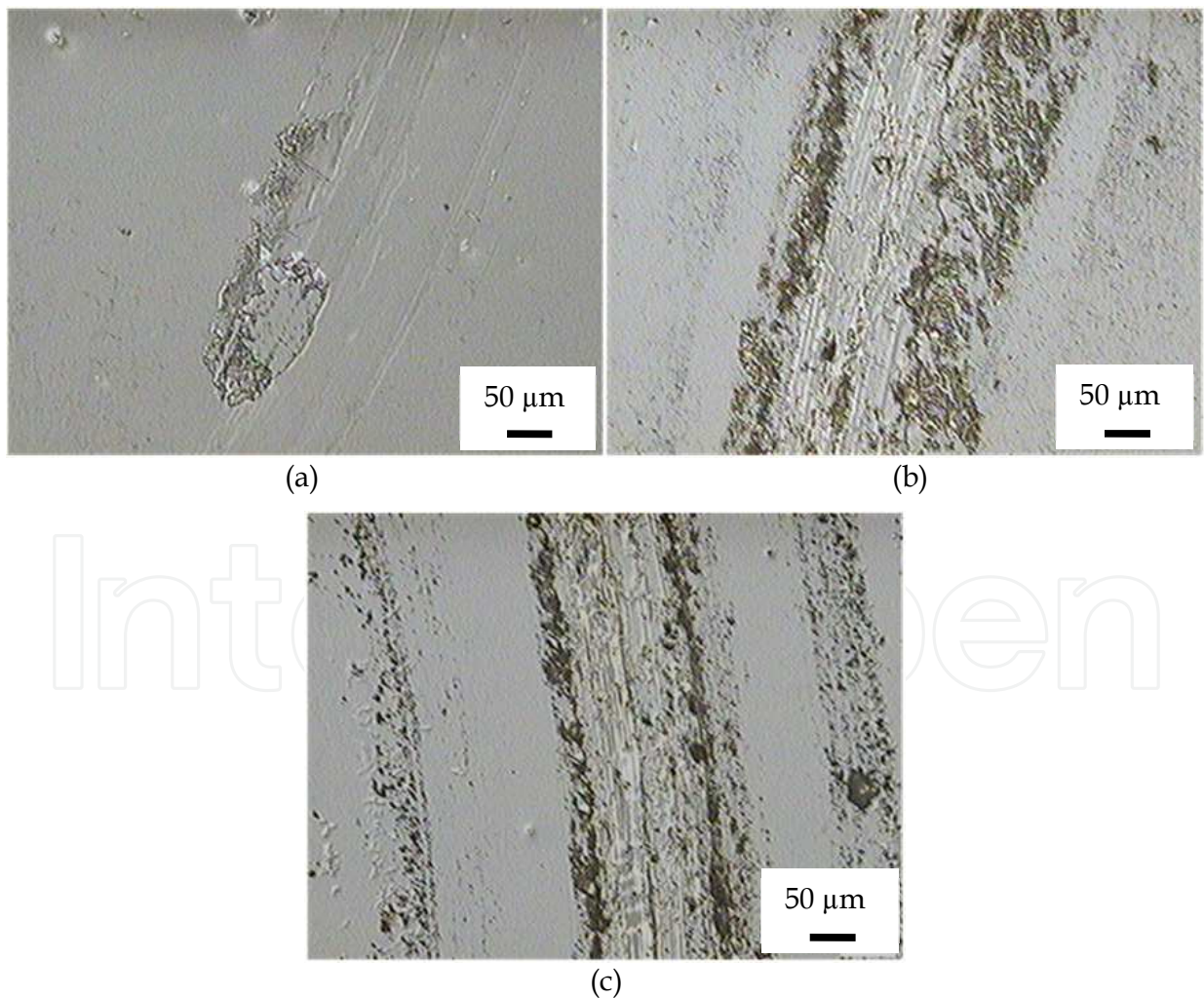


Fig. 6. Photomicrographs of the wear zone after the sliding life test of the coatings: a) Hybrid; b) Hybrid+0.1wAl<sub>2</sub>O<sub>3</sub> on acrylic and c) Hybrid+0.1pAl<sub>2</sub>O<sub>3</sub> on glass.

failure of the coating. As mentioned before, the coating on glass did not fail under sliding conditions, but in Fig. 6c, one can see on the sliding path, some material encrusted due to cold welding of previously removed coating pieces. Comparing the performance of both types of reinforcement, nanoparticles increase friction between the sliding surfaces when the cracking of the coating starts because alumina is harder than the coating and thus the cracking extends until the film completely fails. However, this does not occur with whiskers, which can be attributed to the shape and size of the materials. Whiskers are short discontinuous fibres with a diameter substantially smaller than the length (the whiskers used in this study have a diameter of 2-4 nm and a length of 2800 nm). The length provides more resistance to applied normal forces and instead of cracking only plastic deformation occurs. In this process some material was removed and adhered to the pin due to the local heating caused by friction, making the hybrid material more fluid.

## 2.5 Nanowear testing

Fig. 7 shows scanning probe microscopy (SPM) images of the wear cavities on the coating surfaces after wear testing together along with height profiles of the transverse section. The wear-loss volume was estimated from the depth of the cavities using WSxM software as explained earlier. The profile graphs show that the hybrid material tends to form pile-ups on the cavity edges, generated by the material flow towards the coating surface during the scratch testing (due to the normal and lateral forces applied by the indenter). This is also related to the viscoelastic nature of the hybrid, which is a contribution of the PMMA component; this behaviour will be further explained in a subsequent section. The SiO<sub>2</sub>-PMMA hybrid coating depth profile shows that the edges and walls of the well are more defined than those of the other coatings. The hybrid is a porous material, so when scratched it will tend to compress under the action of the applied normal force during the scanning. If we compare the SiO<sub>2</sub>-PMMA-0.05pAl<sub>2</sub>O<sub>3</sub> coating with the SiO<sub>2</sub>-PMMA, it is possible to observe that the depth of the cavity is smaller than that of the coating without alumina nanoparticles. Another feature that can be observed from the SPM images is that no trace of debris was detected in any of the coatings. The diamond tip does not remove material from the surface; the hybrid is plastically deformed instead. Thus, the nanoparticles at the surface are “displaced” by the tip during scratching, as can be observed for the SiO<sub>2</sub>-PMMA-0.05pAl<sub>2</sub>O<sub>3</sub> coating (Fig. 7-b). The alumina nanoparticles are harder than the coatings, so when the normal force is applied the nanoparticles move within the hybrid film while it is plastically deformed. The SiO<sub>2</sub>-PMMA-wAl<sub>2</sub>O<sub>3</sub> showed a wear-loss volume higher than that of the SiO<sub>2</sub>-PMMA-0.1pAl<sub>2</sub>O<sub>3</sub>. These results can be related to the coating hardness, where the coating with nanowhiskers had the lowest.

Values of wear-loss volume of all hybrid coatings and the acrylic substrate as a function of alumina concentration are presented in Fig. 8. As can be observed, the wear-loss volume of the coatings diminishes as the concentration of alumina nanoparticles increases. At higher contents of nanoparticles the material has more resistance to being compressed by both applied normal and lateral forces. In nanoindentation testing to evaluate hardness, a normal force is applied to the surface of a magnitude necessary to plastically deform the material. In scratch test when lateral and normal forces are applied the material is compressed and flows to the surface, comparable with a hardness test in 2 dimensions. The wear-loss volume of the acrylic substrate without coating is larger by two orders of magnitude than that of all

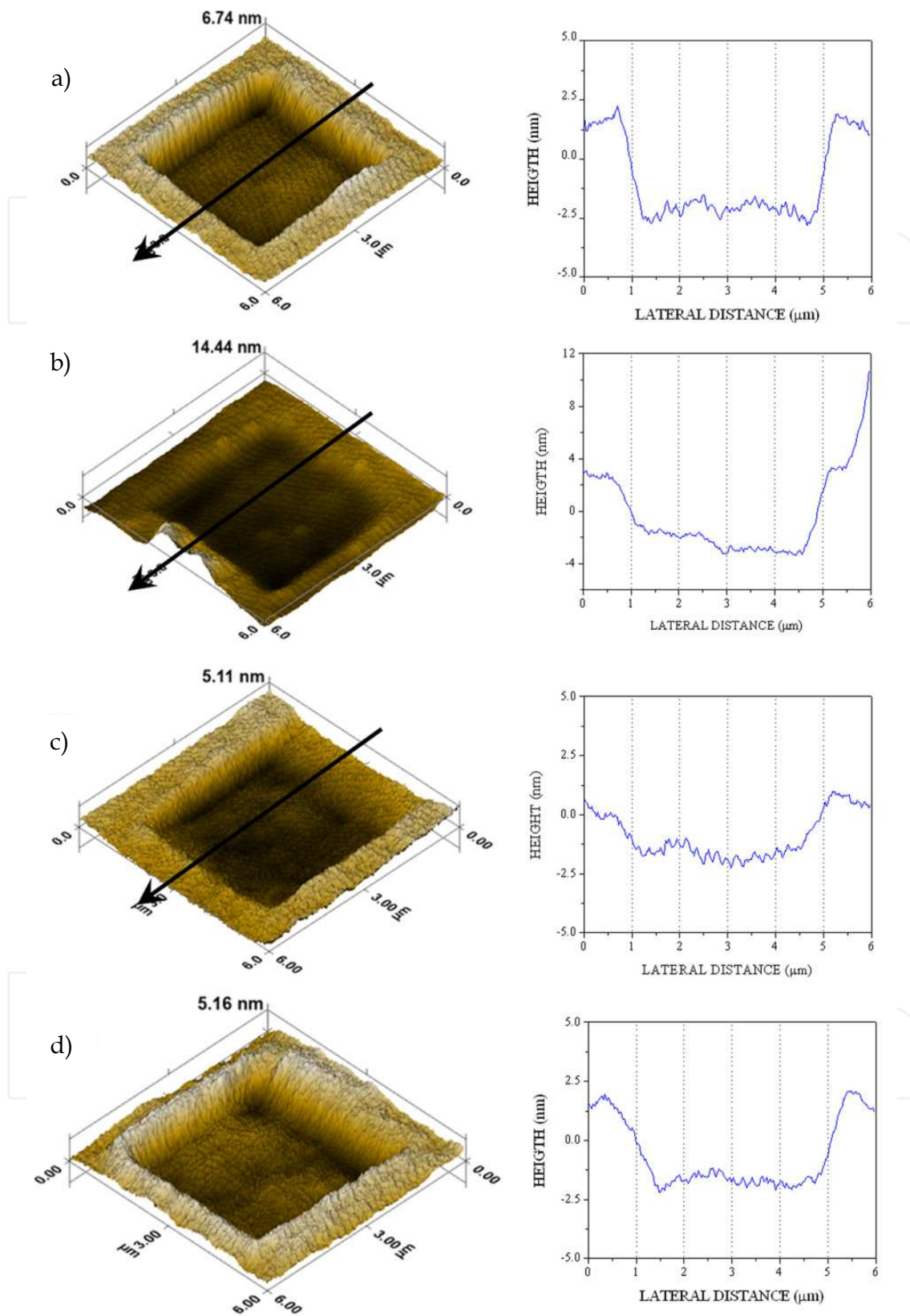


Fig. 7. SPM images of the dwells and the corresponding height profiles after the nanoscratch tests on the surface of: a) Hybrid; b) Hybrid+0.05pAl<sub>2</sub>O<sub>3</sub>, c) Hybrid+0.1pAl<sub>2</sub>O<sub>3</sub> y d) Hybrid+0.1wAl<sub>2</sub>O<sub>3</sub>.

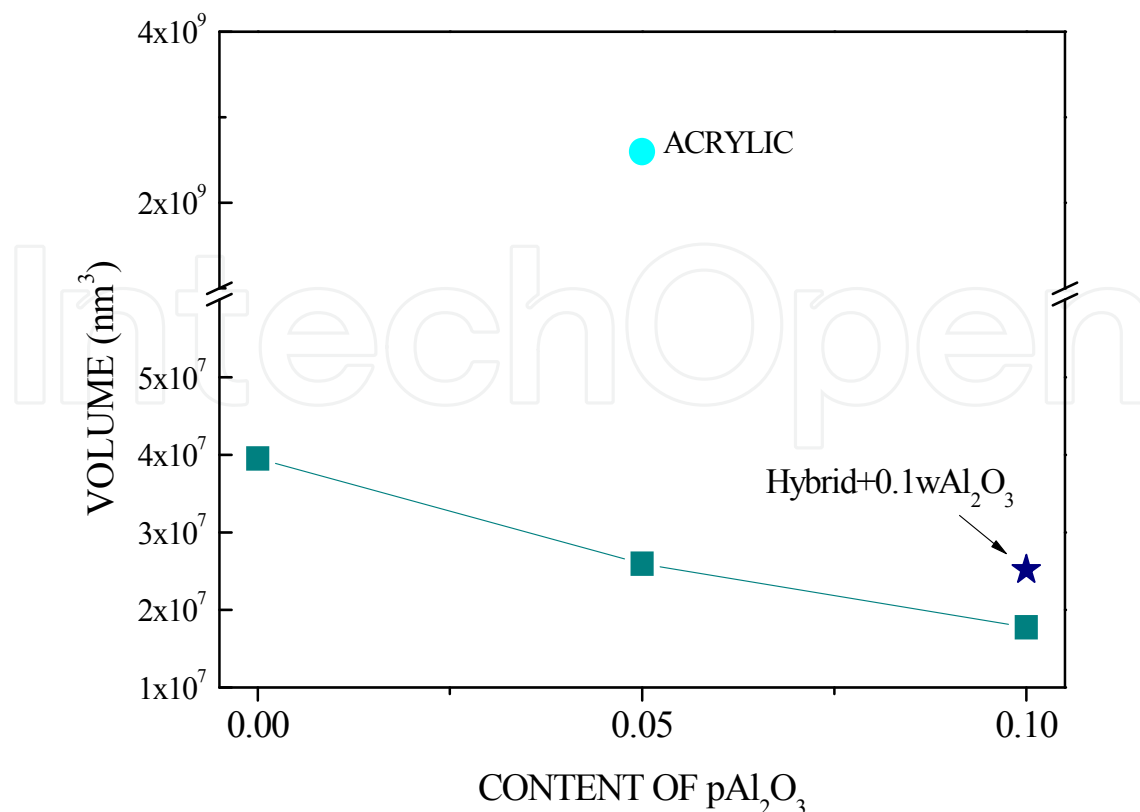


Fig. 8. Wear loss volume of the tested hybrid coatings.

hybrid coatings. The wear-loss volume of the SiO<sub>2</sub>-PMMA-0.05pAl<sub>2</sub>O<sub>3</sub> and SiO<sub>2</sub>-PMMA-0.1wAl<sub>2</sub>O<sub>3</sub> coatings decreases by 32-34%, while for the SiO<sub>2</sub>-PMMA-0.1pAl<sub>2</sub>O<sub>3</sub> coating it drops down by 55%. Therefore, the addition of alumina nanoparticles and whiskers effectively improves the abrasion resistance of the SiO<sub>2</sub>-PMMA hybrid coatings.

### 3. Elastic properties of SiO<sub>2</sub>-PMMA coatings measured by atomic force microscopy

#### 3.1 Material preparation

The hybrid coatings were prepared using TEOS and MMA as precursors and TMSPM as cross linker. For this set of samples a fixed TEOS:MMA composition of 1:0.25 was used, only the TMSPM content was varied from 0.05 to 0.2 molar ratio with respect to TEOS. Corning glass slices were dip coated with the hybrid solutions, and the wet films were dried in an oven. Two different temperatures, 80 and 90°C, were used, along with two drying times, 3 and 6 h. Additional coatings were prepared on silicon substrates for infrared spectra measurements to monitor the hybrid formation. In Table 3, the composition, drying conditions and acronyms to designate each coating are presented.

FT-IR measurements were performed in a Perkin Elmer Spectrum GX. Film thickness of the coatings was measured with a Dektak II Profilometer. Nanoindentation testing was performed on a Hysitron Ubi-1 nanoindenter (Minneapolis, MN). Images of the surfaces to evaluate roughness were taken in a Nanoscope IV Atomic Force Microscope in tapping mode using a silicon rectangular cantilever.

Hybrid composition	Drying conditions		Acronym
	Temperature (°C)	Time (h)	
1:0.25:0.05	80	3	5803
	80	6	5806
	90	3	5903
	90	6	5906
1:0.25:0.2	80	3	20803
	80	6	20806
	90	3	20903
	90	6	20906

Table 3. Characteristics of the synthesized hybrid coatings.

### 3.2 Hybrid characterization

In Fig. 9 the FT-IR spectra of all hybrid coatings are presented. For all coatings a broad band at  $1070\text{ cm}^{-1}$  is present and corresponds to the Si-O-Si bonds, characteristic of silica. This band shows a shoulder at  $\sim 1170\text{ cm}^{-1}$ , formed by the absorption bands at  $1144$  and  $1200\text{ cm}^{-1}$ , corresponding to the C=O and C-O-C bonds, respectively, and indicating the presence of PMMA. It is worth noticing that this shoulder increases in intensity at the highest content of TMSPM in the hybrid solution, thus it can be assumed that the cross linker promotes the formation of PMMA chains. Moreover, the presence of the bands at  $1640\text{ cm}^{-1}$  and near  $1700\text{ cm}^{-1}$  corresponding to the C=C and C=O, respectively, are present, confirming the presence of PMMA in the hybrid material. The band at  $940\text{ cm}^{-1}$  corresponds to uncondensed silanol groups and also the broad band at  $3370\text{ cm}^{-1}$  characteristic of the presence of OH groups.

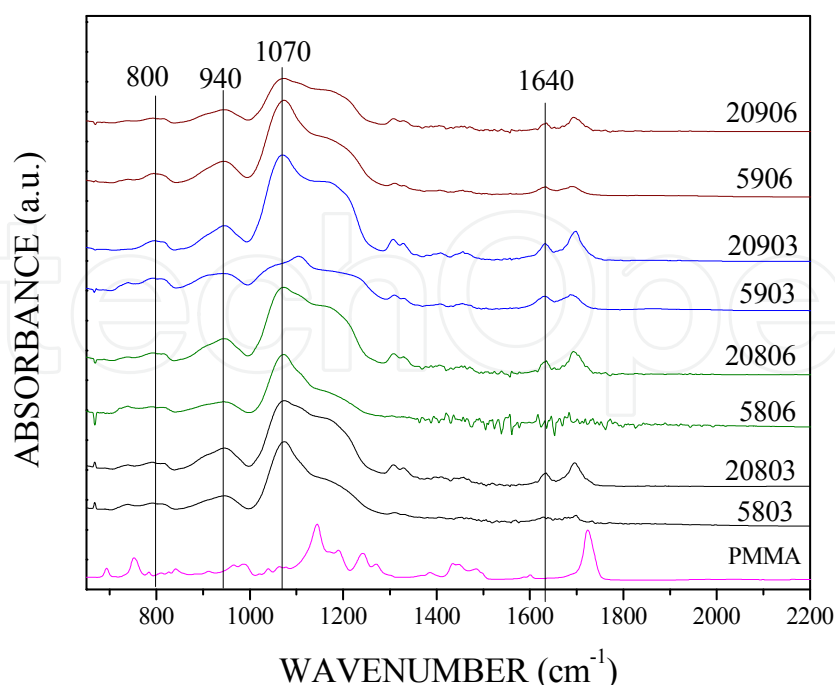


Fig. 9. Infrared spectra of the synthesized hybrid coatings. The spectrum of pure PMMA is also included for comparison.

To evaluate the surface quality of the hybrid coatings, atomic force microscopy (AFM) images in tapping mode were taken in a 5 × 5 μm area. The images and the corresponding values of RMS roughness are presented in Fig. 10. For all measured coatings smooth surfaces were revealed with ultra-low roughness values of less than 1 nm. This feature is of great interest in the fabrication of electronic devices, as extremely flat surface are required as a base for further growth of the thin films that compose the electronic devices.

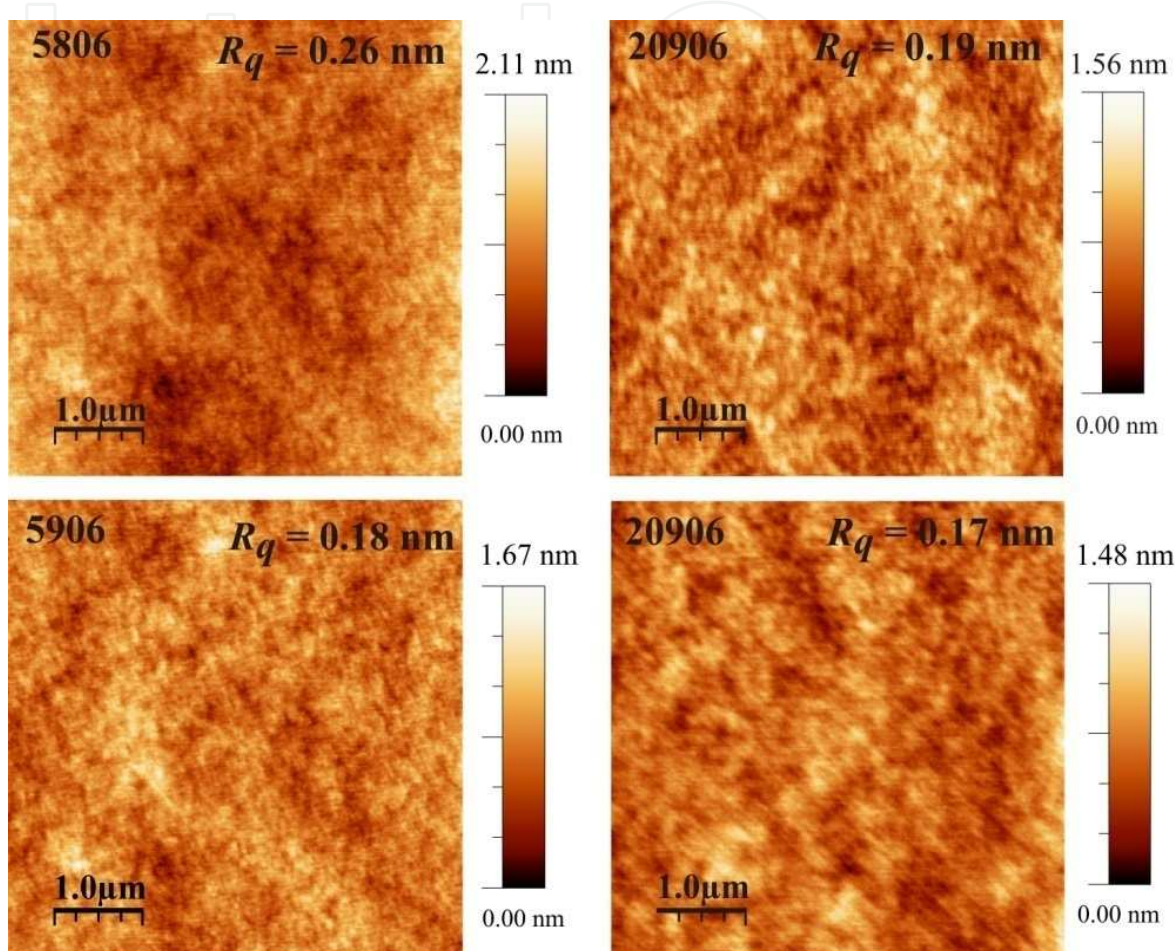


Fig. 10. AFM images of the surface of hybrid coatings.

### 3.3 Nanoindentation testing

One of the characteristics of the hybrid coatings that can be evaluated by nanoindentation is the viscoelastic behaviour, which is defined as follows. A material under an applied stress deforms with a combined behaviour of an elastic solid and a viscous flow. Thus, in viscoelastic materials, the stress-strain relationship depends on time or frequency [Lake, 2004]. Viscoelastic behaviour is also related with materials that have a glass transition temperature similar to thermopolymers such as PMMA. The load-displacement curve of a material with time-dependent response will show a “nose” at the beginning of the unloading curve, as can be seen in Fig. 11a. The material continues to flow under the indenter tip when it is under load; this phenomenon is called creep [Tweedie & Van Vliet, 2006]. A strategy to avoid this type of unloading curve shape is to maintain the maximum load for a certain time, allowing the material to flow viscously until it deforms permanently,

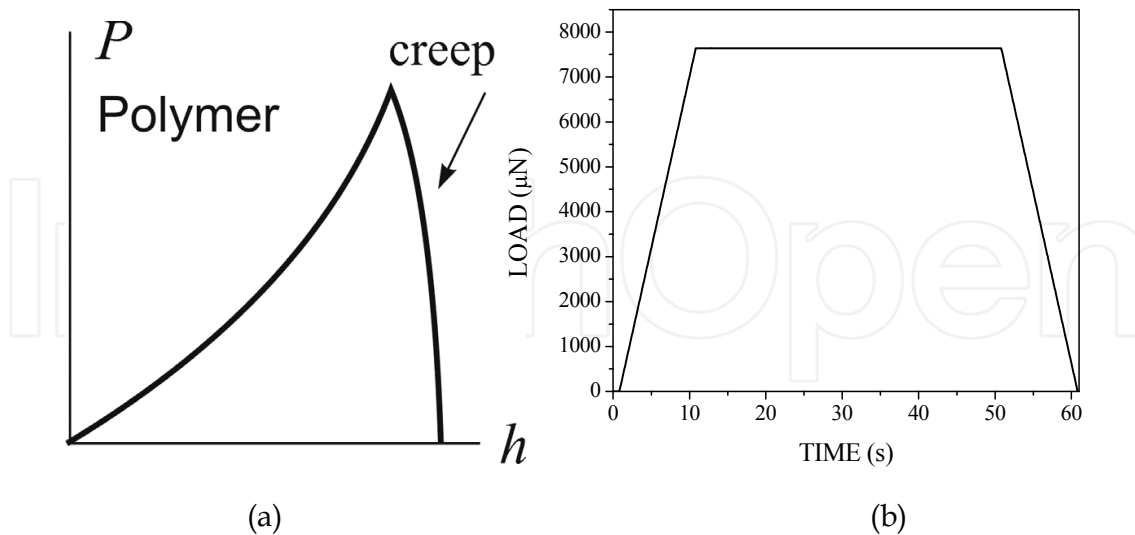


Fig. 11. a) Typical shape of a  $P$ - $h$  curve of a polymer [Fischer-Cripps, 2004] and b) Load-time cycle used for the nanoindentation testing on the hybrid coatings.

and then unload. Then, the Oliver and Pharr method can be applied to extract hardness and reduced modulus. The load-time indentation cycle has a trapezoidal shape (Fig. 11b), in the case of the hybrid coatings the maximum load was maintained for 50 seconds.

### 3.3.1 Hardness and reduced elastic modulus

Film hardness was estimated using the work-of-indentation model [Korsunsky et al., 1998]. In Table 4 the obtained values of  $H_f$  are presented. All the coatings showed film hardness higher than 1.2 GPa, which is several times higher than that for commercial acrylic (~260 MPa, measured by nanoindentation). The hardness values of coatings 20806 and 5903 were not possible to estimate due to an unexpected behaviour of the composite hardness. In a typical nanoindentation test of a coated system, two different behaviours can be observed. When the coating is harder than the substrate, the  $H_c$  values will decrease to values closer than that of  $H_s$ . When the coating is softer than the substrate, the  $H_c$  values will increase near to that of the substrate as the indenter approaches values of  $\beta=1$  [Korsunsky et al., 1998]. The same phenomena occur for reduced modulus [Fischer-Cripps, 2004]. If the hybrid coatings are softer than the glass substrate, then  $H_c$  increases gradually as the indenter goes deeper into the film, as can be seen for the coatings 5803 and 5806 in Fig. 12. The continuous line is the work-of-indentation model fitting. However, for 20806 and 5903 samples, after reaching a maximum,  $H_c$  starts to decrease. This behaviour can be associated with the presence of one or two internal soft layers, thus the hybrid coatings have a gradient of hardness through the thickness. Regarding the hybrid samples (Fig. 12, 20806 and 5903 samples) the data suggests the presence of an external layer on top of a harder layer, causing an increment in the composite hardness. Finally, after the hard layer another soft layer is present and then  $H_c$  decreases. Furthermore, the substrate is harder than the coating, so the hardness values will increase again. However, to observe this behaviour, employment of loads greater than 9000  $\mu\text{N}$  is recommended which it was not possible with the nanoindenter used in this study.

Coating	Film thickness (nm)	Hardness (GPa)
5803	500	1.86
20803	767	1.3
5806	513	1.94
20806	718	--
5903	705	--
20903	744	1.27
5906	446	1.96
20906	1065	1.4

Table 4. Film hardness values of the hybrid coatings obtained by the work-of-indentation model.

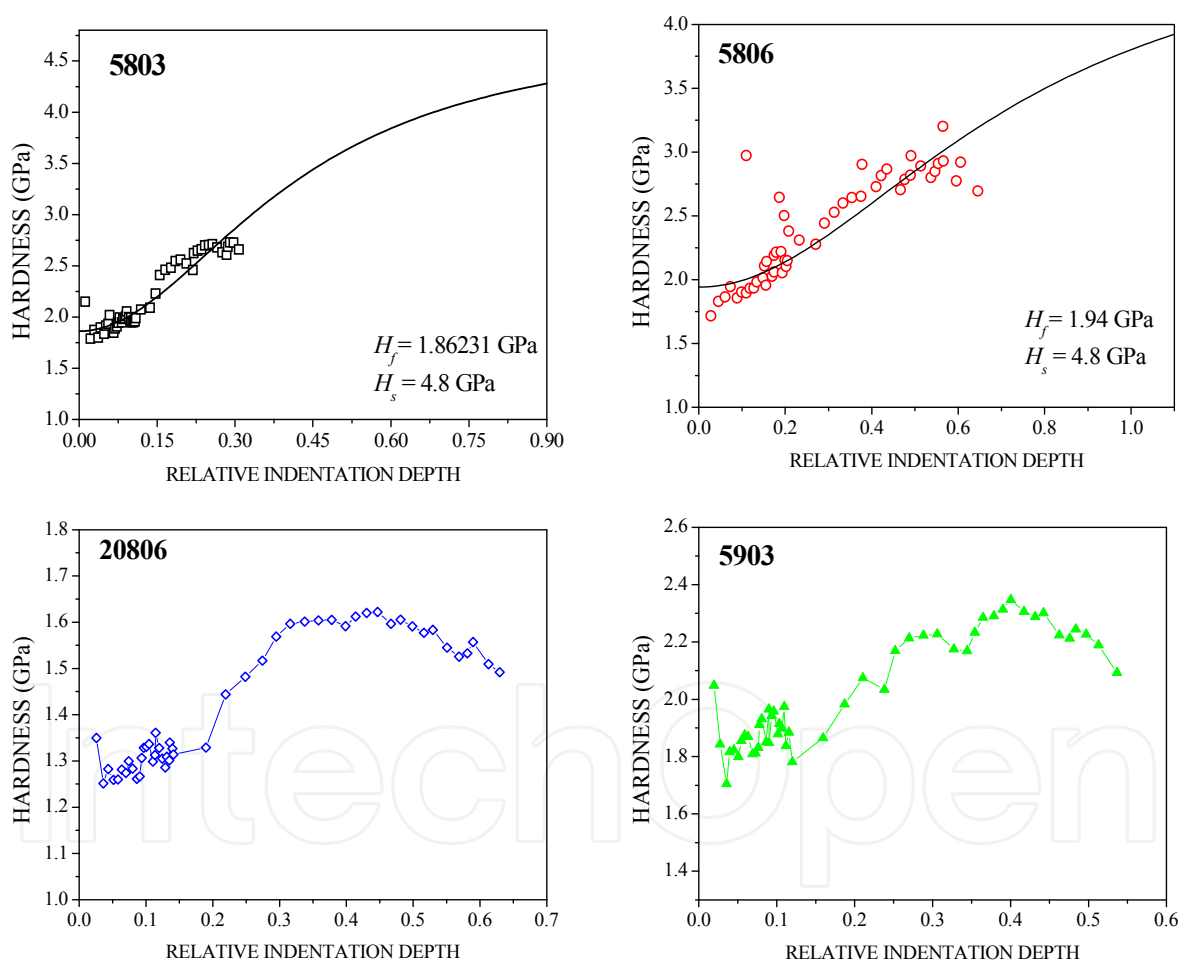


Fig. 12. Composite hardness as a function of the relative indentation depth for some of the hybrid coatings.

In Fig. 13 the reduced modulus as a function of the relative indentation depth is displayed. In the case of the film/substrate system, values of  $E_r$  as a function of the relative indentation depth show the same tendency as the 20806 and 5903 films showed for hardness. The hybrid

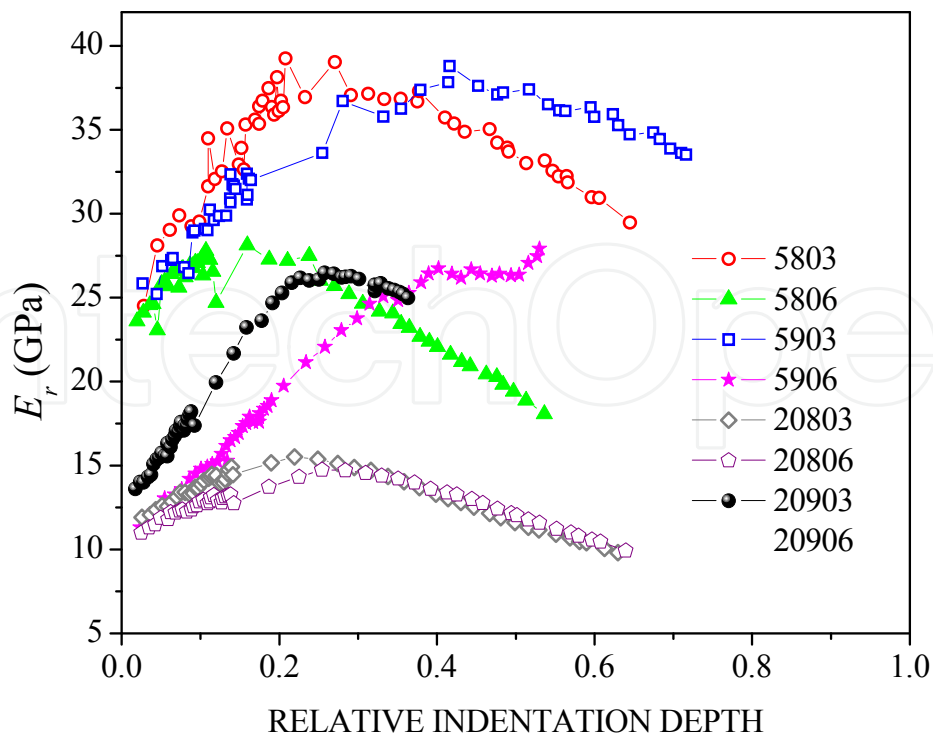


Fig. 13. Reduced modulus of the coating-substrate system as a function of the relative indentation depth.

coatings have elastic modulus gradients through the film thickness. As a result, it was not possible to apply a model to extract the film elastic modulus. Nevertheless, it is possible to observe overall that the films have high values of  $E_r$ , which are higher than that of the PMMA (3.6 GPa) [Cardarelli, 2008]. As with the hardness, the films with higher values of  $E_r$  are those with the lowest content of TMSPM.

### 3.3.2 Creep and stress relaxation

As mentioned above, viscoelastic materials creep under an applied load. This capacity to flow is known as a transitory property, which shows a response in a certain time frame. Creep, creep compliance and stress relaxation are transitory properties of viscoelastic materials [Lake, 2004]. Creep is the time-dependant response to an applied constant stress, and creep compliance is defined as the change in strain as a function of time under an applied constant stress. On the other hand, stress relaxation monitors the change in stress under an applied constant strain [Lake, 2004; Tweedie & Van Vliet, 2006]. To evaluate creep and stress relaxation of the hybrid coatings by nanoindentation, the ISO 14577 standard was employed [Fischer-Cripps, 2004]. This standard makes use of several aspects in instrumented indentation in different penetration depth intervals at macro, micro and nanometric scales and also includes coated systems. In this work we applied the suggested analysis for materials with time-dependant response in order to perform creep and stress relaxation tests.

Creep of a specimen can occur under indentation loading and manifests itself as a change in depth when the applied load is held constant. The relative change in the penetration depth is referred to as the material creep and its value,  $C_{IT}$ , is expressed as:

$$C_{IT} = \frac{h_2 - h_1}{h_1} 100 \quad (2)$$

Where  $h_1$  is the depth at which the maximum applied load begins to be maintained constant, and  $t_1$  is the corresponding time;  $h_2$  is the depth that has been reached at the time,  $t_2$ , when the unloading starts (Fig. 14). As an example of how  $C_{IT}$  is reported:  $C_{IT} = 0.5/10/50 = 2.5$  which means that a creep of 2.5% was determined in a test applying a load of 0.5 N in a time of 10 seconds and maintained constant for 50 seconds.

Stress relaxation  $R_{IT}$  is the relative change in force under an applied constant displacement, thus instead of a constant maximum load, a constant displacement or penetration depth is maintained while the change in force is measured. Stress relaxation is given by:

$$R_{IT} = \frac{F_1 - F_2}{F_1} 100 \quad (3)$$

This equation is very similar to Eqn. (2).  $F_1$  is the force at which the maximum displacement is reached and kept constant and  $F_2$  is the measured force value at time  $t_2$ , the end of the period at which the displacement is maintained constant. A typical curve of displacement as a function of time is depicted in Fig. 14.

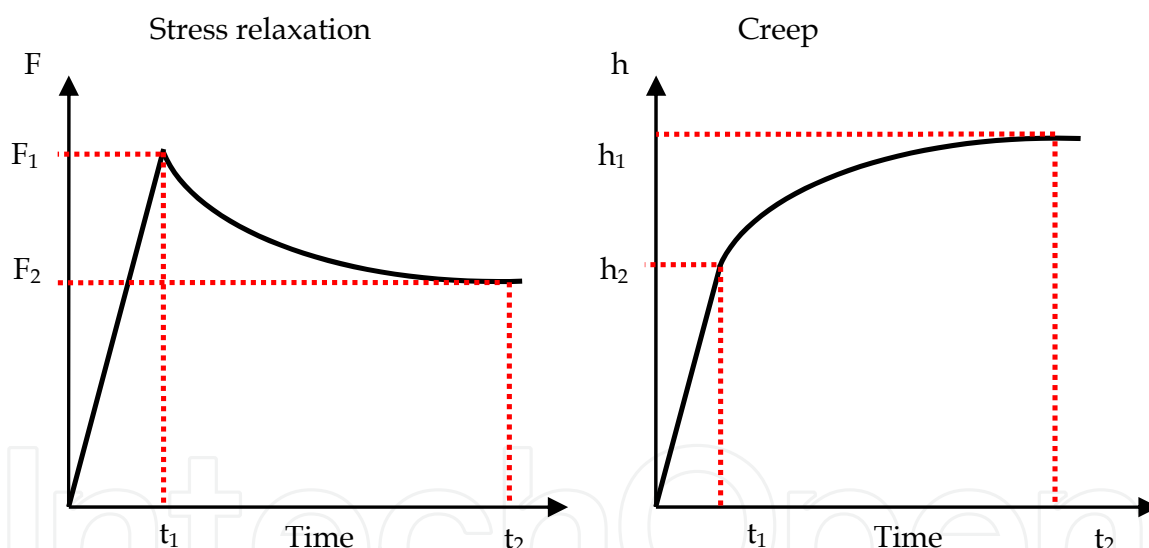


Fig. 14. Schematic representation of the curves of displacement and force as a function of time for creep and stress relaxation tests, respectively.

The results of  $C_{IT}$  and  $R_{IT}$  for the hybrid coatings on glass with 0.2 and 0.05 TMSPM content and standard PMMA as reference are presented in Fig. 15. A series of several indentations varying the maximum load and displacement were performed on all coatings, then the creep and stress relaxation ratios were calculated from all the indentations performed on each coating. For both  $C_{IT}$  and  $R_{IT}$  the hybrid coatings showed values lower than that of the PMMA, which is at least twice as high. However, there is no a marked difference between the different contents of TMSPM or drying temperatures and time. The creep values are more dispersed than those for stress relaxation (i.e., the error bars are smaller for stress

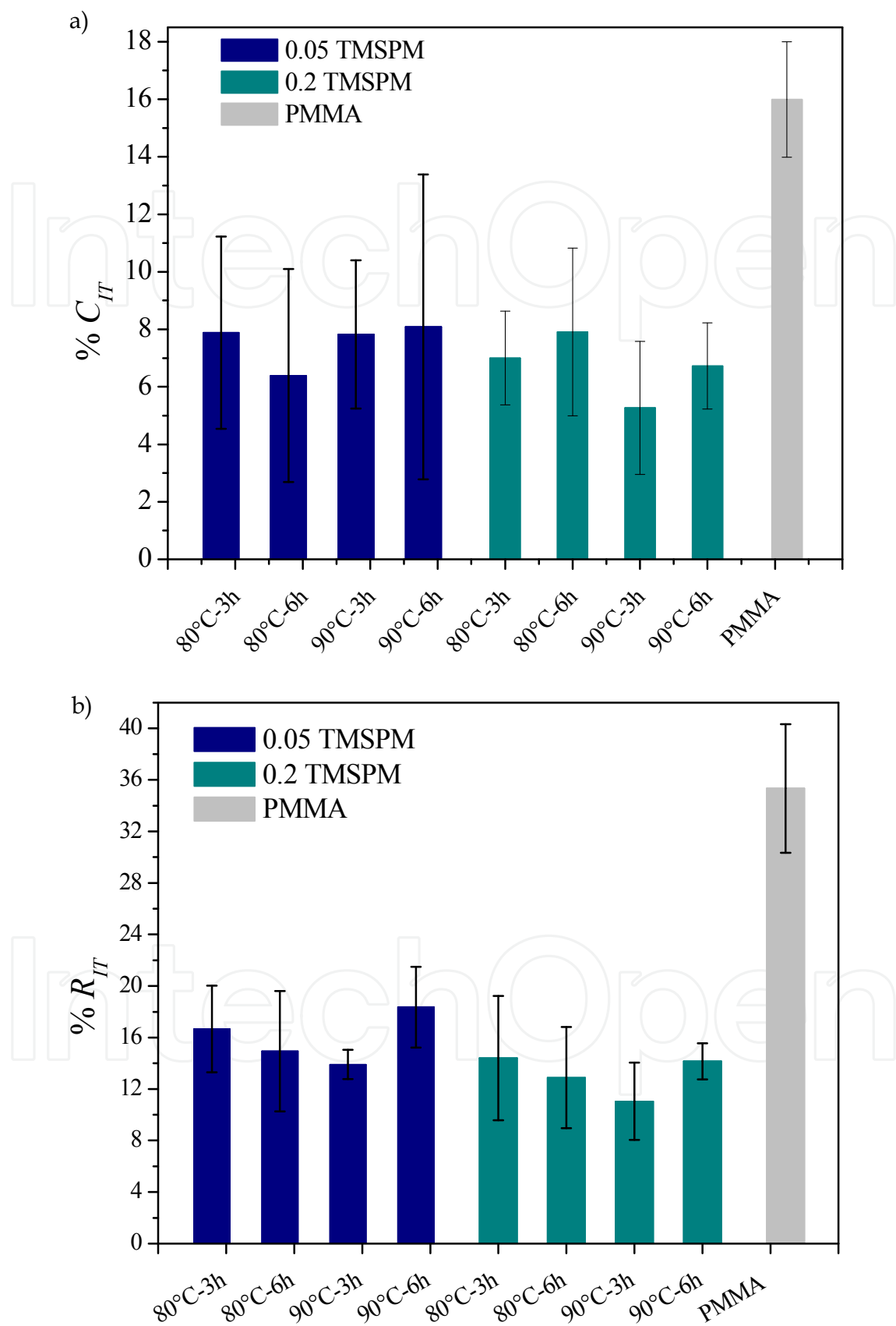


Fig. 15. a) Creep and b) Stress relaxation results of the hybrid coatings on glass.

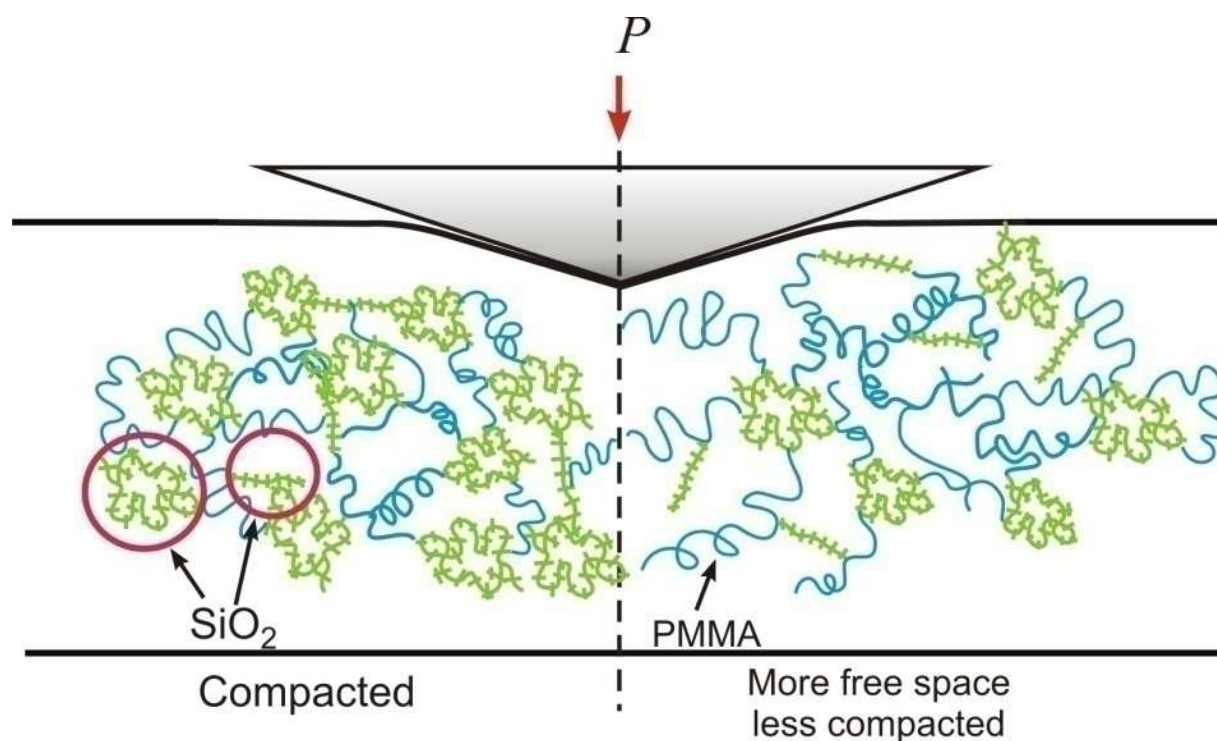


Fig. 16. Schematic representation of the hybrid conformation and distribution of phases when a load is applied.

relaxation). This distinctive behaviour can be associated with localized phenomenon of the hybrid structure or phase distribution. Since creep is the material's capacity to flow, this value will depend upon the chain coiling and available space to the chain to unroll when it is under load. In Fig. 16 a schematic representation of the possible phase distribution of the organic and inorganic phases which are responsible of the viscous flow of the hybrid coating is presented.

### 3.4 Atomic Force Acoustic Microscopy (AFAM)

During the last decades acoustic force microscopy has been employed to image differences in elastic properties and for detection of defects, applied in a wide range of fields, including physics, non-destructive testing and medicine. This technique is based on transmission and reflection of ultrasonic waves [Rabe, 2006]. The acoustic microscope is a confocal system, this is that focus occurs when both acoustic waves travel through the specimen and are detected by the lenses. Contrast in the image depends on the acoustic impedance and consequently in the elastic constants of the specimen. This technique has a restricted lateral resolution of about the half of the value of the wavelength [Briggs, 1985]. With the invention of atomic force microscopy (AFM), other techniques that combined its characteristic with ultrasonic imaging methods were developed, such as ultrasonic force microscopy (UFM), scanning atomic force microscopy (SAFM), ultrasonic atomic force microscopy (UAFM) and atomic force acoustic microscopy (AFAM). The advantage of combining AFM with ultrasonic techniques is that the probe has a tip with a radius less than 100 nm, allowing high image resolution. Thus tip contact radius is several orders of magnitude lower than the acoustic wavelength, which defines the local resolution [Briggs, 1985]. In AFAM a

transducer placed under the sample sends longitudinal waves through the sample causing out-of plane ultrasonic vibrations of the surface. These vibrations are coupled with the AFM cantilever tip generating flexural vibrations of the probe [Kopycinska-Müller, et al., 2007]. This technique can be used to obtain images by mapping the vibration amplitude of the sample surface. In this case, the probe is excited at a fixed frequency near to its resonance frequency. Depending on the local contact stiffness the resonance frequency will change and consequently the vibration amplitude of the work frequency will change, which will also be reflected in contrast differences in amplitude images. These images provide qualitative information about differences in stiffness in regions of the sample surface [Kopycinska-Müller, et al., 2007; Rabe, 2006].

### 3.4.1 AFAM spectroscopy mode

For AFAM measurements, the information of the contact resonance can be collected in either, step-by-step or sweep mode. In the former, the wave generator changes its output frequency from an initial set value to a final one and this type of measurement is used to analyze a single point on the surface sample. In sweep mode, a frequency interval is scanned in 0.5 seconds, producing a great number of spectra. Contact resonance frequencies are measured as a function of the cantilever static deflection, which is affected by the tip geometry. If the tip has a different geometry from that of a flat indenter, then the increment in static force will lead to an increment in the contact area between the tip and the sample and therefore in the contact stiffness. Thus, the resonance frequency will change to higher values [Kopycinska-Müller et al., 2007].

In our analysis, the tests were performed on a modified Dimension 3000 atomic force microscope in the Fraunhofer Institut for Non-destructive Testing in Saarbruecken, Germany. A diagram of the microscope and associated equipment is presented in Fig. 17. This set-up is used to excite and detect AFAM contact-resonance frequencies in order to measure the local elastic constants of the material. The sample is placed on an ultrasonic transducer that emits longitudinal waves and the produced out-of-plane surface vibrations are detected by the cantilever beam when it is in contact with the surface. These vibrations are the contact resonance frequencies, and they are a consequence of the tip-sample interactions that modify the boundary conditions for the vibrating cantilever. The tip-sample interactions depend on the static force  $F_C = k_C \times \Delta z$  applied to sensor tip by the cantilever deflection  $\Delta z$  and on the attractive tip-sample forces, such as electrostatic and adhesion forces [Rabe et al., 2002]. In this set-up the contact-resonance frequencies are measured as a function of the static deflection of the cantilever.

Since the tip of the cantilever probe is in contact with the surface applying a certain load, only a small volume of the sample determines the elastic contact forces. According to the Hertzian model [Johnson, 1985] a contact area with a radius of:

$$a = \sqrt[3]{\frac{3F_C R}{4E^*}} \quad (4)$$

is formed when an isotropic sphere of radius  $R$  contacts an elastic isotropic flat surface. Here,  $E^*$  is the reduced elastic modulus and is given by:

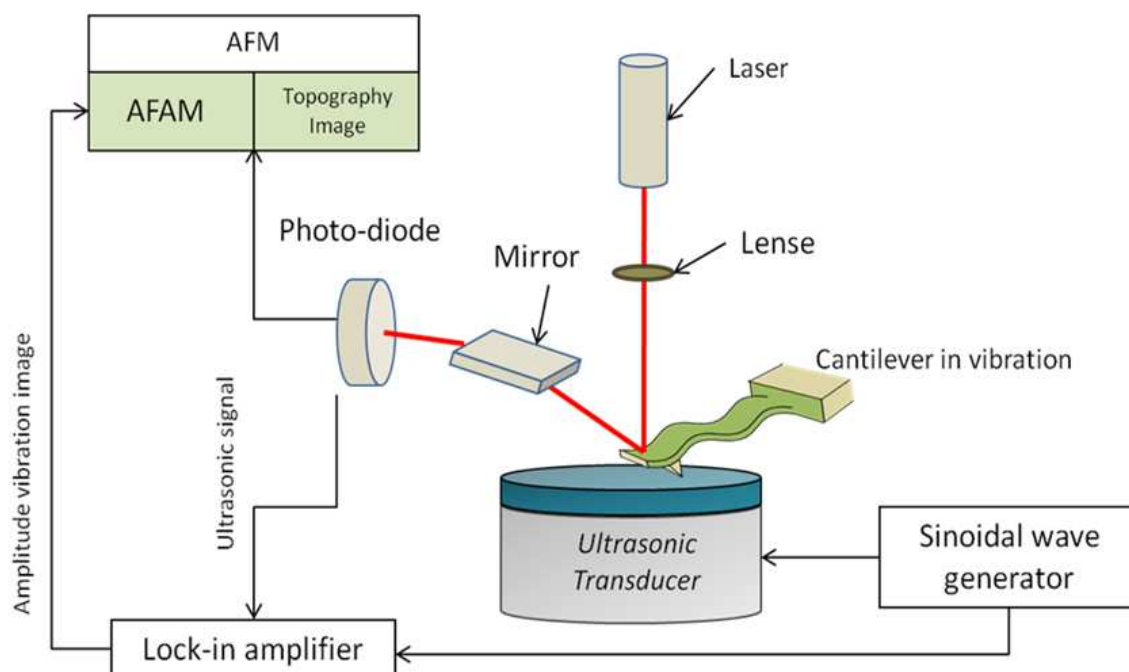


Fig. 17. Experimental set-up of AFM for the acoustic spectroscopy [Rabe, 2006].

$$\frac{1}{E^*} = \frac{(1 - \nu_s^2)}{E_s} + \frac{(1 - \nu_T^2)}{E_T} \tag{5}$$

where  $E_s$ ,  $E_T$ ,  $\nu_s$ , and  $\nu_T$  are the Young’s moduli, the Poisson’s ratios of the surface and the tip, respectively. At small vibration amplitudes the tip-sample forces can be linearized and are represented by a contact stiffness  $k^*$

$$k^* = \sqrt[3]{6E^* R F_C}$$

However, the tip shapes often deviate from that of a sphere [Kopycinska-Müller et al., 2007; Rabe et al., 2002]. In the case of a flat punch, the radius of the punch  $R_p$  is equal to the contact radius  $a_C$ , and the contact stiffness  $k^*$ , which is no longer load-dependent, is given by:

$$k^* = 2R_p E^* \tag{6}$$

For anisotropic solids an indentation modulus  $M$  is introduced and it is calculated from the single-crystal elastic constants. Then the equation for the reduced elastic modulus  $E^*$  can be replaced by:

$$\frac{1}{E^*} = \frac{1}{M_s} + \frac{1}{M_T} \tag{7}$$

were  $M_s$  and  $M_T$  are the indentation modulus of the sample and the tip, respectively. The tip shape can be characterized by evaluating the contact resonances for reference samples with known indentation modulus. The elastic properties can be evaluated using the following equation by comparative measurements:

$$E_s^* = E_r^* \left( k_r^* / k_s^* \right)^m \quad (8)$$

Here,  $r$  and  $s$  refer to the reference and the unknown sample, respectively, and  $m$  describes the tip geometry. For a flat punch  $m = 1$  and for a spherical tip  $m = 3/2$ .

### 3.4.2 Determination of the resonance frequencies of the hybrid coatings

The set of samples analyzed by AFAM in spectroscopy mode were 5806, 20806, 5906 and 20906 together with standard samples of fused silica and PMMA for comparison and calibration. NCL silicon probes from Nanosensors with rounded tips and spring constants  $k_c$  ranging from 33 to 34 N/m were used. The free resonance frequencies of this cantilever were 159.2 KHz, 989 KHz and 2710.5 KHz for the first, second, and third flexural mode, respectively. The contact-resonances were taken at a static cantilever deflection  $p_f = 40$  nm, which means a static force of 1360 nN was applied to the hybrid surfaces. The resonance frequencies recorded for hybrid sample 5806 are presented in Fig. 18. The standards were used to estimate the shape and elastic moduli of the tip. The first, second and third contact resonances were obtained for this purpose. For the analysis of the results two Labview programs were used. The first allows calculation of the tip position and the contact stiffness with or without considering the lateral forces from two flexural modes of contact resonances. The second Labview program determines the tip position using two flexural modes of contact resonance from two reference samples. It calculates the contact stiffness from the unknown sample using only one contact resonance. For the experiment a sequence for measurement was established as follows: fused silica, PMMA, 5806, 20806, 5906, 20906, fused silica and PMMA. The results for the contact resonance frequencies of the first and second flexural mode for each sample are presented in Fig. 19. These values were used to estimate the contact stiffness of the hybrid coatings. It can be seen that sample 5906 shows the highest values of all hybrid coatings, and it is also close to that of the fused silica for both flexural modes. In the case of sample 20806, the values of the second flexural mode are considerably different from each other, thus only the first flexural mode contact resonance frequency values were used to estimate the contact stiffness of this sample.

In order to calculate the contact stiffness it is necessary to determine the position of the cantilever tip along the length of the probe. For this, the measured values of the contact resonance frequencies of the first and second mode of the fused silica and PMMA were used. The estimated position was  $L_1/L = 0.949$ , where  $L$  is the probe length and  $L_1$  is the tip position. With this value the contact stiffness of the hybrid coatings surfaces was determined, and the results are presented in Table 5.

As was mentioned earlier, coating 5906 showed the highest value of contact resonance frequency, and the contact stiffness is also the highest of all samples. It is worth mentioning that the contact stiffness of fused silica is  $k^* = 2639$  N/m, thus in the case of this coating, the surface must be constituted primarily of a dense silica layer. This coating also showed the highest measured value of hardness in nanoindentation testing. The  $k^*$  values presented in Table 5 were obtained using both first and second flexural mode contact resonance frequencies. For sample 20806 the contact stiffness was measured considering only the first flexural mode, and the calculated value was 949.6 N/m, which is similar to that obtained for the sample with the same TMSPM content but dried at 90°C (Sample 20906). The hybrid

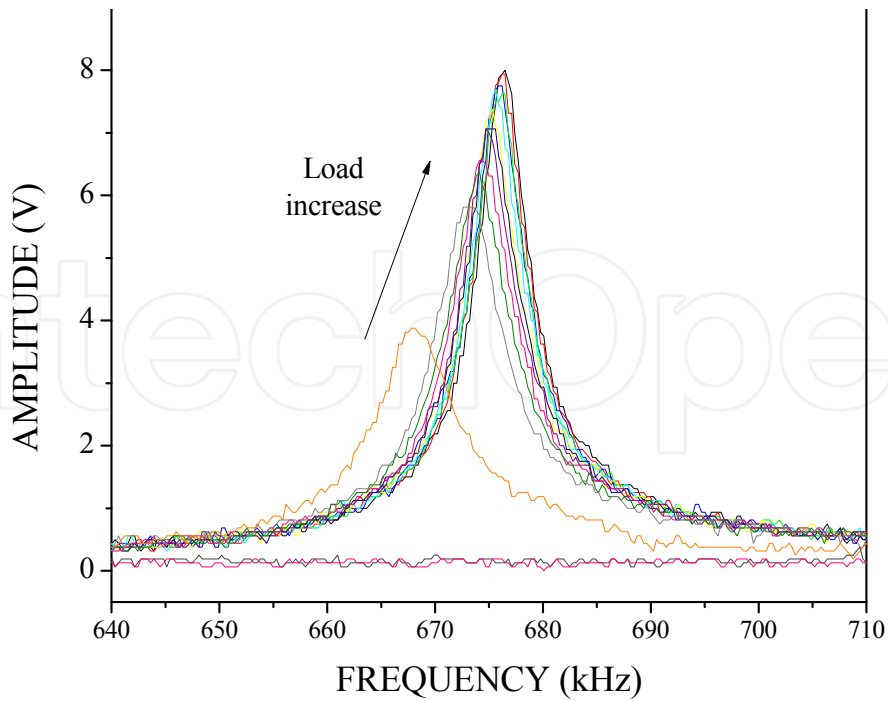


Fig. 18. Recorded contact resonance spectra of the 5806 coating during cantilever loading.

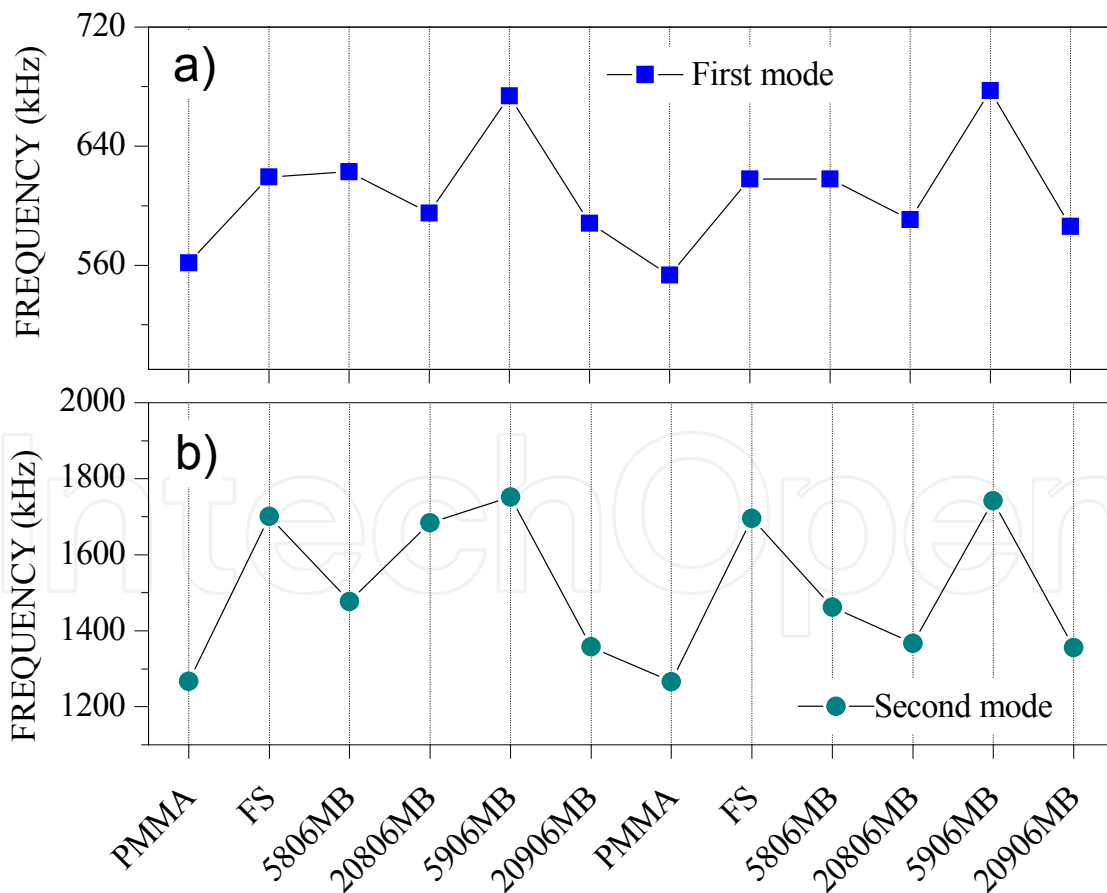


Fig. 19. Variation of the contact resonance frequencies of a) first and b) second flexural modes as a function of measurement order.

Sample	Contact stiffness, $k^*$ N/m
5806	1328
20806	--
5906	2593.5
20906	964

Table 5. Contact stiffness values of the analyzed hybrid samples.

with 0.2 molar ratio of TMSPM showed lower values of contact stiffness. This result can be associated to the more PMMA chains in the surface. According to FT-IR spectra, a major content of the crosslinker promotes the formation of PMMA. Thus, the hybrid coating will show elastic properties similar to that of the polymer.

### 3.4.3 AFAM imaging mode

AFAM images of the hybrid coatings were taken in a modified Nanoscope IV Dimension 3000. A silicon cantilever coated with Cr/Pt (Budget sensors), with a spring constant of 3 N/m and a tip radius of 20-25 nm, was used. The samples measured were those analyzed by AFAM spectroscopy. Images of a 1x1  $\mu\text{m}$  area of the hybrid film surfaces were taken and are presented in Fig. 20. This is a complementary analysis the spectroscopy. Even though it is a qualitative analysis it is very useful to observe differences in stiffness of the sample surface. The first step is to find the local contact resonance frequency of the surface and then tune the cantilever near this frequency. Afterwards, the vibration amplitude of the surface is scanned, and the changes in stiffness will be represented as contrast between dark and bright zones. When the surface has lower stiffness than the measured local stiffness, it will show as dark zones; otherwise when the stiffness is higher it will show as bright zones. Amplitude images show details that are not always perceptible in the topography images. The phase images show the different components of the sample surface, which for the case of hybrid coatings are silica and PMMA. Then the phase and amplitude images reveal structural details regarding the local stiffness of the analyzed zones.

As mentioned earlier when discussing the AFM topography images, the hybrid coatings have an ultra-low surface roughness and a smooth surface. The resonance frequencies used to tune the cantilever for each sample are presented in Table 6, these values were taken measuring the local contact resonance frequency at a single point on the coating surface. Then with AFAM structural details of the PMMA and silica component distribution were revealed. Samples 5806 and 20806 phase images show distinct distribution of bright and dark regions in the phase images and some black spots, which can be pores. Sample 5906 does not show a clear distribution of shapes either in the phase or amplitude image, probably because of a more random distribution of silica and PMMA. In the case of sample 20906, zones with different contrast are visible showing a particular morphology of elongated "beans" whit sizes of 30 to 80 nm. These images demonstrate the formation of a material where both phases are distributed in regions of less than 100 nm. This provides the material with its high transparency, ultra low roughness and low friction coefficient. Further studies on coatings with different contents of PMMA will be interesting to observe if the materials arranges itself in a specific shape and size.

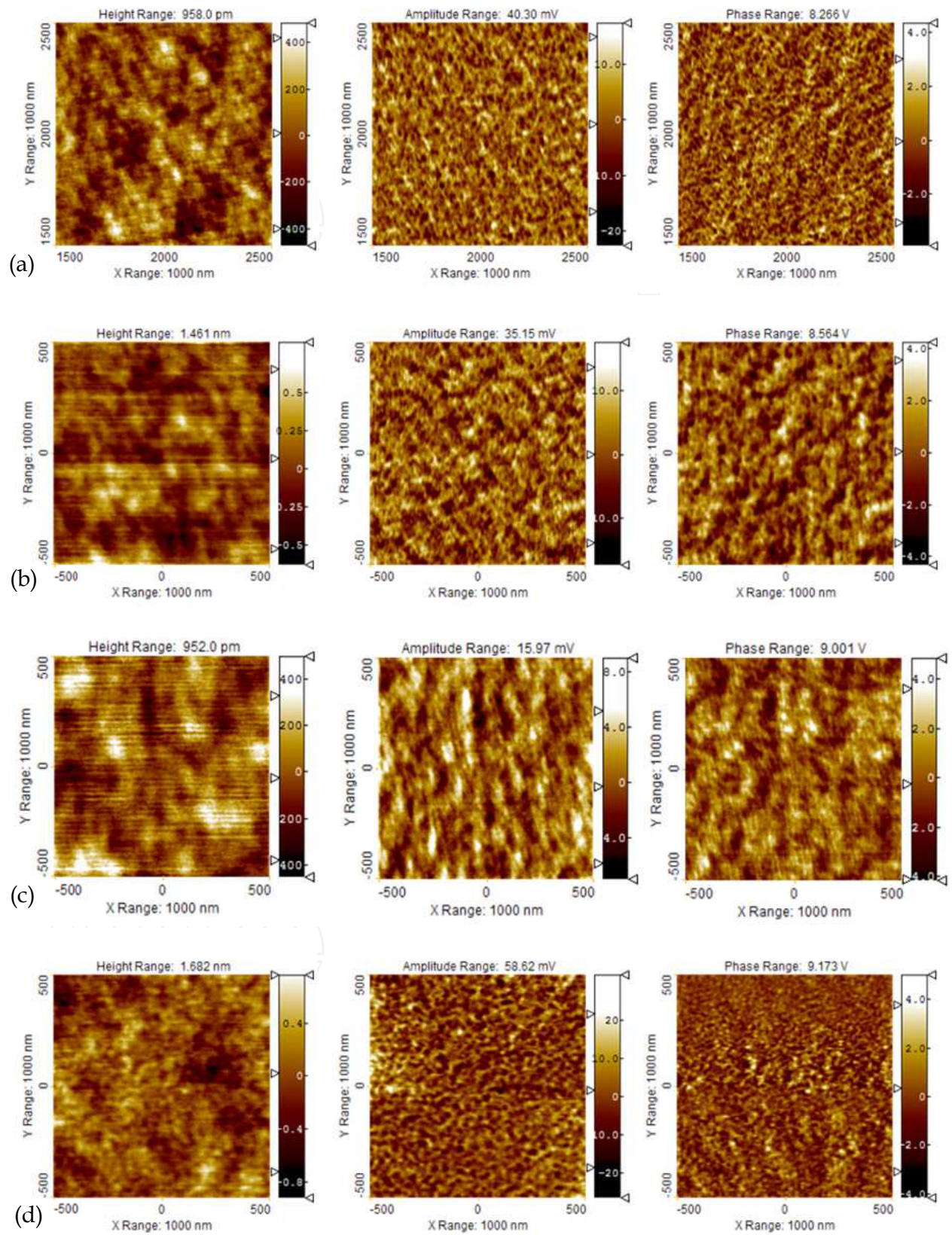


Fig. 20. Height, amplitude and phase images of the coatings: a) 5806, b) 20806, c) 5906 and d) 20906.

Sample	Cantilever Excitation frequency (kHz)
5806	339.84
2806	338.86
5906	340.82
20906	339.84

Table 6. Frequency values used to tune the cantilever for AFAM imaging.

#### 4. Conclusion

The addition of  $\text{Al}_2\text{O}_3$  nanoparticles and whiskers improve the wear resistance behaviour of the hybrid material even though the hardness of the coatings does not show an increase. The hybrid coating  $\text{SiO}_2\text{-PMMA-0.1wAl}_2\text{O}_3$  was the one with the best performance in the sliding life test resisting the whole test without failing. In general, in the nanoscratch testing all the coatings have better wear resistance than that of the acrylic substrate, showing values of wear loss volume two orders of magnitude lower than that of the substrate. Moreover, the concentrations of nanoparticles and whiskers used in this study improved the wear resistance behaviour and transparency of the films was maintained.

According to the AFAM spectroscopy mode results, the TMSPM content and drying temperature of the hybrid coatings have an important effect on the contact stiffness of the hybrid coating surfaces. The hybrid coating with a TMSPM content of 0.5 and dried at  $90^\circ\text{C}$  for 6 hours showed the highest value of contact stiffness, near to that of the fused silica standard. This result is in good agreement with the nanoindentation hardness, in which the same coating showed the highest hardness value. In general, the coatings with a TEOS:TMSPM molar ratio of 1:0.5 have higher values than those of the coatings with a TMSPM content of 0.2. According to the FT-IR spectra results, these results are associated with the capability of the TMSPM to promote the formation of PMMA chains. In this respect, the AFAM imaging testing showed that the silica and PMMA phases are homogeneously distributed, forming nanometric domains of each component. This can be related to the transparency of the film and the smooth surfaces of the hybrid coatings with roughness values of less than 2 nm.

#### 5. Acknowledgments

Authors thank Prof. Dr. W. Arnold and Dr. U. Rabe from Fraunhofer Institut for Non-Destructive Testing in Saarbruecken, Germany for their support in AFAM spectroscopy mode measurements and Dr. Francisco Javier Espinoza Beltrán from Cinvestav-Unidad Querétaro for his help in the AFAM imaging testing.

#### 6. References

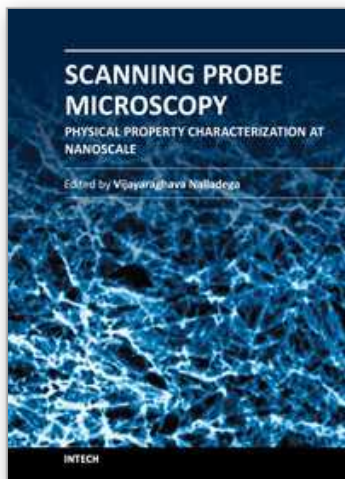
- Alvarado-Rivera, J., Muñoz-Sadaña, J., & Ramírez-Bon, R. (2010). Nanoindentation testing of  $\text{SiO}_2\text{-PMMA}$  hybrid films on acrylic substrates with variable coupling agent content. *Journal of Sol-Gel Science and Tehcnology*, Vol. 54, No. 3 , pp. 312-318, ISSN 0928-0707.

- Alvarado-Rivera, J., Muñoz-Saldaña, J., Castro-Beltrán, A., Quintero-Armenta, J. M., Almaral-Sánchez, J., & Ramírez-Bon, R. (2007). Hardness and wearing properties of SiO<sub>2</sub>-PMMA hybrid coatings reinforced with Al<sub>2</sub>O<sub>3</sub> nanowhiskers. *Physica Status Solidi C*, Vol. 14, No. 11, pp. 4254-4259, ISSN 1862-6351.
- Briggs, A. (1985). *An Introduction to Scanning Acoustic Microscopy*, Royal Microscopical Society Handbook 12. Oxford University.
- Cardarelli, F. (2008). *Materials Handbook: a concise desktop reference, 2nd Edition*. New York, NY: Springer, ISBN-13 9781846286681.
- Fischer-Cripps, A. (2004). *Nanoindentation*. New York, United States of America: Springer-Verlag, ISBN 0-387-22045-3.
- Hay, J., & Pharr, G. (2000). Instrumented Indentation Testing. In H. Kuhn, & D. Medlin, *ASM Handbook Vol.8 Mechanical Testing and Evaluation* (pp. 232-243). Ohio, United States of America: ASM International, ISBN 978-0871703897.
- Horcas, I., Fernández, R., Rodríguez, J., Colchero, J., Gomez-Herrero, J., & Baro, A. (2007). WSXM: A software for scanning probe microscopy and a tool for nanotechnology. *Review of Scientific Instruments*, vol. 78, No. 1, 013705, ISSN 0034-6748.
- Huang, H.-H., Orlor, B., & Garth, L. (1985). Ceramers: Hybrid Materials Incorporating Polymeric/Oligomeric Species with Inorganic Glasses by a Sol-Gel Process 2. Effect of Acid Content on the Final Properties. *Polymer Bulletin*, Vol. 14, pp. 557-564, ISSN 557-564.
- Johnson, K. (1985). *Contact Mechanics*. Cambridge: Cambridge University Press.
- Kopycinska-Müller, M., Caron, A., Hirsekorn, S., Rabe, U., Natter, H., Hempelmann, R., et al. (2007). quantitative Evaluation of Elastic Properties of Nano-Crystalline Nickel Using Atomic Force Acoustic Microscopy. *Zeitschrift für Physikalische Chemie*, Vol. 222, No. 2-3, pp. 471-498, ISSN 004-3336.
- Korsunsky, A., McGurk, M., Bull, J., & Page, T. (1998). On the hardness of coated systems. *Surface and Coatings Technology*, Vol. 99, No. 1-2, pp. 171-183, ISSN 0257-8297.
- Lake, R. (2004). Viscoelastic measurements techniques. *Review of Scientific Instruments*, Vol. 75, No. 4, 797-810, ISSN 0034-6748.
- Oliver, W., & Pharr, G. (1992). An improved technique for determining hardness and elastic modulus using load and displacement sensing indentation experiment. *Journal of Materials Research*, Vol. 7, No. 6, pp. 171-183, ISSN 0884-2914.
- Rabe, U. (2006). Atomic Force Acoustic Microscopy. In B. Bhushan, & H. Fuchs, *Applied Scanning Probe Methods II* (pp. 37-90). Germany: Springer-Verlag, ISBN 978-3-540-26242-8.
- Rabe, U., Amelio, S., Kopycinska, M., Hirsekorn, S., Kempf, M., Göken, M., et al. (2002). Imaging and measurement of local mechanical material properties by atomic force acoustic microscopy. *Surface and Interface Analysis*, Vol.33, No.1, 65-70, ISSN 1096-9918.
- Sanchez, C., & Ribot, F. (1994). Design of hybrid organic-inorganic materials synthesized via Sol-Gel chemistry. *New Journal of Chemistry*, Vol. 18, No. 10, pp. 1007-1047, ISSN 0959-9428.
- Sanchez, C., Julián, B., Belleville, P., & Popall, M. (2005). Applications of hybrid organic-inorganic nanocomposites. *Journal of Materials Chemistry*, Vol. 15, No. 35-36, pp. 3559-3592, ISSN 0959-9428.

- Schmidt, H. (1985). New type of non-crystalline solids between inorganic and organic materials. *Journal of Non-Crystalline Solids*, vol. 73, No. 1-3 , pp. 681-691, ISSN 0022-3093.
- Tweedie, C., & Van Vliet, K. (2006). Contact creep compliance of viscoelastic materials via nanoindentation. *Journal of Materials Research*, Vol. 21, No. 6 , 1576-1589, ISSN 0884-2914.

IntechOpen

IntechOpen



## Scanning Probe Microscopy-Physical Property Characterization at Nanoscale

Edited by Dr. Vijay Nalladega

ISBN 978-953-51-0576-3

Hard cover, 242 pages

**Publisher** InTech

**Published online** 27, April, 2012

**Published in print edition** April, 2012

Scanning probe microscopy (SPM) is one of the key enabling tools for the advancement for nanotechnology with applications in many interdisciplinary research areas. This book presents selected original research works on the application of scanning probe microscopy techniques for the characterization of physical properties of different materials at the nanoscale. The topics in the book range from surface morphology analysis of thin film structures, oxide thin layers and superconducting structures, novel scanning probe microscopy techniques for characterization of mechanical and electrical properties, evaluation of mechanical and tribological properties of hybrid coatings and thin films. The variety of topics chosen for the book underlines the strong interdisciplinary nature of the research work in the field of scanning probe microscopy.

### How to reference

In order to correctly reference this scholarly work, feel free to copy and paste the following:

J. Alvarado-Rivera, J. Muñoz-Saldaña and R. Ramírez-Bon (2012). Elastic and Nanowearing Properties of SiO<sub>2</sub>-PMMA and Hybrid Coatings Evaluated by Atomic Force Acoustic Microscopy and Nanoindentation", Scanning Probe Microscopy-Physical Property Characterization at Nanoscale, Dr. Vijay Nalladega (Ed.), ISBN: 978-953-51-0576-3, InTech, Available from: <http://www.intechopen.com/books/scanning-probe-microscopy-physical-property-characterization-at-nanoscale/elastic-and-nanowearing-properties-of-sio2-pmma-hybrid-coatings-evaluated-by-atomic-force-acoustic-m>

**INTECH**  
open science | open minds

### InTech Europe

University Campus STeP Ri  
Slavka Krautzeka 83/A  
51000 Rijeka, Croatia  
Phone: +385 (51) 770 447  
Fax: +385 (51) 686 166  
[www.intechopen.com](http://www.intechopen.com)

### InTech China

Unit 405, Office Block, Hotel Equatorial Shanghai  
No.65, Yan An Road (West), Shanghai, 200040, China  
中国上海市延安西路65号上海国际贵都大饭店办公楼405单元  
Phone: +86-21-62489820  
Fax: +86-21-62489821

© 2012 The Author(s). Licensee IntechOpen. This is an open access article distributed under the terms of the [Creative Commons Attribution 3.0 License](#), which permits unrestricted use, distribution, and reproduction in any medium, provided the original work is properly cited.

IntechOpen

IntechOpen